24th COBEM - 2017

24th ABCM International Congress of Mechanical Engineering
December 3-8, 2017, Curitiba, PR, Brazil

COBEM-2017-0097
NUMERICAL INVESTIGATION AT LOW REYNOLDS NUMBERS OF THE GALLOPING INSTABILITY OF A CIRCULAR CYLINDER WITH A SPLITTER PLATE EMPLOYING A SPECTRAL/HP FINITE ELEMENT METHOD

Robin L. G. Basso
Gustavo R. S. Assi
Dept. Naval Arch. & Ocean Eng., Escola Politecnica, University of Sao Paulo, Brazil
robinbasso@usp.br
g.assi@usp.br

Reinaldo M. Orselli
Fabio Saltara
Dept. Mechanical Eng., Escola Politecnica, University of Sao Paulo, Brazil
fsaltara@usp.br
reiorselli@gmail.com

Abstract. *This paper presents a numerical investigation of the forces acting on a circular cylinder of diameter D fitted with a rigid, fixed splitter plate of length D and thickness $l = 0.1D$, submerged in a steady flow of velocity U at an incidence angle α. Fluid forces are employed in a quasi-steady model of the dynamics system based on the classical theory of galloping instability. We first remember the range of validity of the quasi-steady theory in each degree of freedom (plunge and torsion) in a view to justify the size our geometry. Then we describe the numerical method we used, and our results for Reynolds numbers equal to 60 and 200. Secondly, we visualize the flow behavior around the body and note that it behaves as a bluff body. Then we focus on the steady aerodynamic coefficients for each angle of attack, and investigate the way to better extract the values for their derivatives. Afterwards, we show that regarding the Den Hartog's criterion for the stability of classical galloping (stability in plunge), there is no potential instability for the system at both Reynolds numbers. The validity of a quasi-steady approach to model a complex fluid-structure interaction problem is also discussed.*

Keywords: *Quasi-steady theory, galloping, Den Hartog's criterion, spectral/hp FEM, DNS.*

1. INTRODUCTION

The dynamic instabilities of a body due to fluid structure interactions are highly presents in the nature, and their complexities have given birth to severals analytics models in order to describe these phenomenons. Here we focus on the flow past a cylinder fixed to a rigid splitter-plate and his Quasi-Steady galloping model. This model is presented in section (2.) as a simple spring-supported, damped linear partial equation, responding to a aerodynamic force. This resulting force is a function of the aerodynamic coefficient (according to the dimension which is studied i.e. C_y, C_x, or C_M) which is, the only unknown. Indeed, all the others parameters are functions of structural properties and flow characteristics.

Therefore, we devote this paper to the investigation of these coefficients. They can be extracted either experimentally or numerically, and we choose here to present a numerical way. The methodology we decided to use is a spectral/hp, finite elements method (Karniadakis and Sherwin, 2004) which computes a direct numerical simulation (DNS) of the incompressible Navier Stokes equations over the fluid domain (section 3.). To do so, we used the software Nektar++ (Cantwell *et al.*, 2015), and it allowed us to compute these simulations for a Reynolds number of 60 and 200: the limit of flow's bi-dimentional behaviour (Zdravkovich, 1997). Besides, we used Gmsh (Geuzaine and Remacle., 2009) to generate our different meshes, and Paraview (Ahrens *et al.*, 2005), for the visualisations and post-processing. In order to validate the method's convergency in this practical case, we ran series of tests (for the p and $h-type$ convergency) prior to compute our simulations and extract the results. In a future work, we will extend these investigations first for the aerodynamic moment coefficient, and then for higher Reynolds number by using the quasi-3D theory.

This article have been written as part of the PhD thesis of Robin L. G. Basso, and it must be considered as a preliminary investigation of it. Indeed, this work will contribute to feed first a galloping model in plunge, then in torsion, to finally be extended to a two dimensional flutter model (torsion and plunge).

It is also plan to compare these final results through experimental investigation, for the same range of Reynolds numbers.

2. GALLOPING FONOMENON

Let's consider our geometry (cylinder fitted to the splitter plate) immersed in a flow of intensity U_{flow} and density ρ, as shown in Fig. 1. As the cylinder oscillates (over y for instance), the orientation of the incoming flow over the geometry changes and becomes U. And since the body isn't rotationally symmetric in relation to the z axis, the resulting forces F_L and F_D oscillates as well. So we can describe the lift force F_L as the component which acts perpendicularly to the mean flow U and the drag force F_D as the one which acts parallel to U. As:

$$F_D = \frac{1}{2}\rho U^2 D C_D \tag{1}$$

$$F_L = \frac{1}{2}\rho U^2 D C_L \tag{2}$$

Where C_L and C_D are the aerodynamics coefficients of lift and drag respectively, D is the diameter of the cylinder, and $\dot{y}$ is the vertical velocity of the geometry. We express α, the angle of attack and U, the actual flow velocity as:

$$\alpha = \arctan\left(\frac{\dot{y}}{U_{flow}}\right) \tag{3}$$

$$U = \sqrt{\dot{y}^2 + U_{flow}^2} \tag{4}$$

Since we want to work with the resulting forces F_y and F_x, we must transform them in the (x, y) basis. We proceed as follow:

$$\begin{bmatrix} F_x \\ F_y \end{bmatrix} = \begin{bmatrix} \cos(\alpha) & -\sin(\alpha) \\ \sin(\alpha) & \cos(\alpha) \end{bmatrix} \begin{bmatrix} F_D \\ F_L \end{bmatrix} \tag{5}$$

And we finally obtain the couple of resulting forces that we are going to use in our equations of motion:

$$F_x = \frac{1}{2}\rho U_{flow}^2 D C_x \quad ; \quad C_x = \frac{U^2}{U_{flow}^2}\left(C_D\cos(\alpha) - C_L\sin(\alpha)\right) \tag{6}$$

$$F_y = \frac{1}{2}\rho U_{flow}^2 D C_y \quad ; \quad C_y = \frac{U^2}{U_{flow}^2}\left(C_D\sin(\alpha) + C_L\cos(\alpha)\right) \tag{7}$$

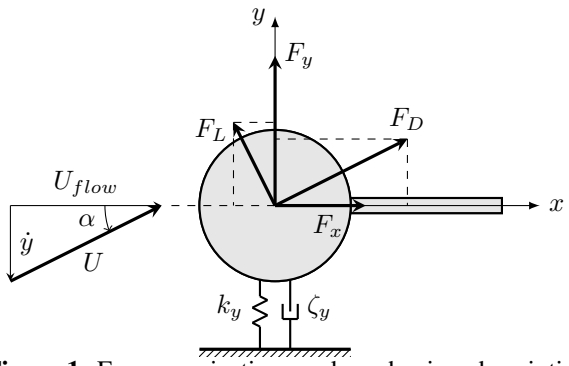

Figure 1: Forces projections and mechanism description.

We also define the damping factor due to dissipation within the structure as ζ_y, and the structural stiffness of the spring as k_y. The values associated to these quantities are fixed and determined from a concrete problem. Here we are going to study the problem oscillating vertically, so we will focus on the F_y expression.

We choose to size our geometry in a way that the ration $D/L = 2$ (height over chord), in a view to applicate safely the quasi-steady theory in both vertical and torsional dimensions. See section (2.2).

2.1 Quasi-Steady theory

The essence of this theory comes from that we consider the case that our flow's time scale T_{Fluid} is much higher that our solid's time scale T_{Solid}. In this case, the influence of the fluid oscillation will not have so much influence on the solid's movement. Analogically, according to Blevins (2001), this assumption is only valid if the frequency of total periodic components of fluid force is well above the vibration frequency of the structure: $f_s \gg f_n$. Where f_s is the shedding frequency and f_n is the natural frequency of vibration.

We assume this condition true and go ahead expending our quantities in power series. For small angle of attack, we got:

$$\alpha = \frac{\dot{y}}{U_{flow}} + \mathcal{O}\left(\alpha^2\right) \tag{8}$$

$$U = U_{flow} + \mathcal{O}\left(\alpha^2\right) \tag{9}$$

$$C_y(\alpha) = C_y|_{\alpha=0} + \left.\frac{\partial C_y}{\partial \alpha}\right|_{\alpha=0} \alpha + \mathcal{O}\left(\alpha^2\right) \tag{10}$$

Here we neglected the terms proportional to α^2 and higher powers of α: $\mathcal{O}\left(\alpha^2\right)$. We can now express the motion of the system over the y dimension (since we are first looking for plunge stability), in function of the resulting forces and the linearised terms. The Eq. (6) to Eq. (8) implies the following equation of one dimension motion for the spring-supported, damped model responding to the vertical aerodynamic force:

$$m\ddot{y} + 2m\zeta_y\omega_y\dot{y} + k_y y = F_y \tag{11}$$

$$m\ddot{y} + 2m\omega_y\left(\zeta_y - \frac{\rho U D}{4m\omega_y}\left.\frac{\partial C_y}{\partial \alpha}\right|_{\alpha=0}\right)\dot{y} + k_y y = \frac{1}{2}\rho U^2 D\, C_y|_{\alpha=0} \tag{12}$$

Here m describes the mass per unit length, including the added mass, and $\omega_y = 2\pi f_y = \sqrt{k_y/m}$ describes the natural frequency in radian per second (and f_y is the natural frequency of plunge in cycles).

2.2 The Den Hartog criterion

If, for commodity, we express Eq. (11) in function of the net damping factor of vertical motion ζ_T:

$$\zeta_T = \zeta_y - \frac{\rho U D}{4m\omega_y}\left.\frac{\partial C_y}{\partial \alpha}\right|_{\alpha=0} \tag{13}$$

We obtain the solution for Eq. (11) of the form:

$$y = \frac{-\frac{1}{2}\rho U^2 D\, C_y|_{\alpha=0}}{k_y} + A_y e^{-\zeta_T\omega_y t}\sin\left[\omega_y\sqrt{1-\zeta_T^2}\,t + \phi\right] \tag{14}$$

So we obtain that the vertical oscillations will increase or decrease in time depending of the sign of ζ_T. Since the only variable in the expression of ζ_T (see Eq. (13)) is the slope of the curve of C_y around zero, we can make explicit the divergency criterion of the solution:

$$\lim_{t\to\infty}|y| \to \begin{cases} \text{potentially} \quad \infty \quad \text{if} \quad \left.\frac{\partial C_y}{\partial \alpha}\right|_{\alpha=0} > 0 \\ 0 \quad \text{if} \quad \left.\frac{\partial C_y}{\partial \alpha}\right|_{\alpha=0} < 0 \end{cases} \tag{15}$$

This is the Den-Hartog (1956), criterion of stability. In section (5.1), we presents the curves of C_y and the slope of its derivative in function of the angle of attack.

Regarding the validity of this criterion, Blevins (2001), claims that this theory is applicable safely at reduced velocity $U^* = U/f_n D$ above 20, for a rectangular section of ratio $L/D = 2$. When according to Bearman *et al.* (1987) , this theory is applicable safely at reduced velocity above 30, considering a square prism.

Concerning the torsional validity, Nakamura and Mizota (1975), tried to show the correlation between the unsteady aerodynamic damping coefficient for torsional motion, k_a, and the Quasi-Steady moment derivative, $\partial C_M/\partial\alpha$ depending of the hinge point's position. The region of same sign fairly fit for small ratio L/D (≤ 2). Where L is the chord.

3. NUMERICAL APROACH

3.1 The spectral/hp elements method

The spectral/hp elements method (Cantwell *et al.*, 2015) is used in a wide range of applications including biomedical flows and separated/bluff body flows of relevance to offshore engineering and vehicle aerodynamics, where direct numerical simulations are required. This method is whilst:

- a finite element method of $h-type$: the piecewise polynomial basis functions is fixed and any change of discretisation to enhance accuracy is done by means of a mesh refinement,

- a finite element method of $p-type$: the partitioning of domain is kept fixed and any change of discretisation is introduced through a modification in polynomial degree P,

- a spectral element method: the high accuracy of the spectral methods (spectral methods approximate the solution by a truncated series of global basis functions) is combined to the geometric flexibility of the finite element method.

Since it is a finite elements based method, we used the same continuous (C^0) Galerkin formulation to derive the weak form of the partial differential equation to be solved: the incompressible Navier-Stokes equations.

In section (3.2) we show how and why we choose to work with an expansion polynomial of degree $P = 6$ for each field.

3.1.1 Incompressible Navier-Stokes equations

Here we work with the set of governing equation for viscous Newtonians fluids governed by:

$$\begin{cases} \dfrac{\partial \mathbf{u}}{\partial t} + \mathbf{u}.\nabla\mathbf{u} = -\nabla p + \nu\nabla^2\mathbf{u} \\ \nabla.\mathbf{u} = 0 \end{cases} \quad \Leftrightarrow \quad \begin{cases} \dfrac{\partial \mathbf{u}}{\partial t} + \mathbf{u}.\nabla\mathbf{u} = -\nabla p + \dfrac{1}{Re}\nabla^2\mathbf{u} \\ \nabla.\mathbf{u} = 0 \end{cases} \tag{16}$$

Where $\mathbf{u} = [u, v]^T$ is the velocity, p is the specific pressure (including density) and ν the kinematic viscosity. Here we normalised the intensity of the incoming flow $U = 1$, and since we choose $D = 1$, we can equivalently work with the second part of the Eq. (16).

3.2 Computational domain and boundary conditions

The angle of attack variation was made statically, i.e., each simulation was performed with a fixed angle and the geometry orientation remained unchanged, as shown in Fig. (2). In order to avoid the divergence of the the Courant-Friedrichs-Lewy (CFL) condition, we used a conformal, partially structured mesh where the characteristics are presented in Tab. (2).

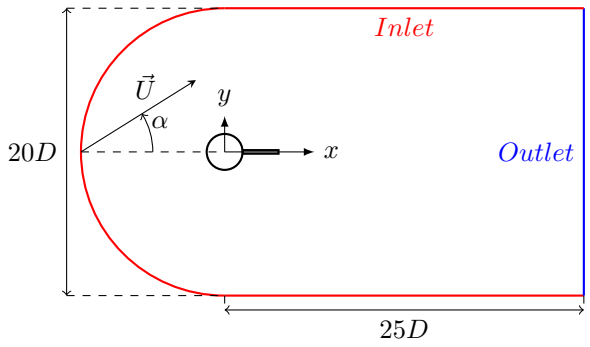

Figure 2: Domain dimensions (not scaled).

Table 1: Boundary conditions type in the domain regions.

Physical Group	Field	Type	Value
Inlet	u	Dirichlet	$U.\cos(\alpha)$
	v	Dirichlet	$U.\sin(\alpha)$
	p	Neumann	0
Outlet	u	Neumann	0
	v	Dirichlet	0
	p	Dirichlet	0
Cylinder walls (no slip)	u	Dirichlet	0
	v	Dirichlet	0
	p	Neumann	0

Table (1) summarise the type of boundary conditions we implement overs the different regions of the hole domain.

In order to chose the right order of interpolation P, we realised a test of convergency. We compared the C_x and C_y coefficients for $\alpha = 0°$, $Re = 200$ and $P = 2$ to 7. Figure (3) shows the values of these coefficients (C_x represented by the dash-dot line and C_y by the solid line) in function of the dimensionless time $t = 160$ that we used in all our simulations. We clearly see that C_x reach its mean convergency value for $P \geq 6$ and C_y for $P \geq 3$, which is clearer in Fig. (4) where we calculated the mean of the signal over the last period for each value of P. This analyse allows us to

Table 2: Technical characteristics of the meshes.

Name	Width	Length	Elements	Vertices	Type	Order
Mesh 2	16D	28D	2138	7994	Quadrilateral	2
Mesh 3	20D	35D	2797	10558	Quadrilateral	2
Mesh 4	20D	35D	4869	18636	Quadrilateral	2

chose and validate properly the maximum polynomial order P we used in our simulations for $Re = 60$ and $Re = 200$. Indeed, we expect that as the flow behaviour is less critical for $Re = 60$, we can use the same value of P for both cases.

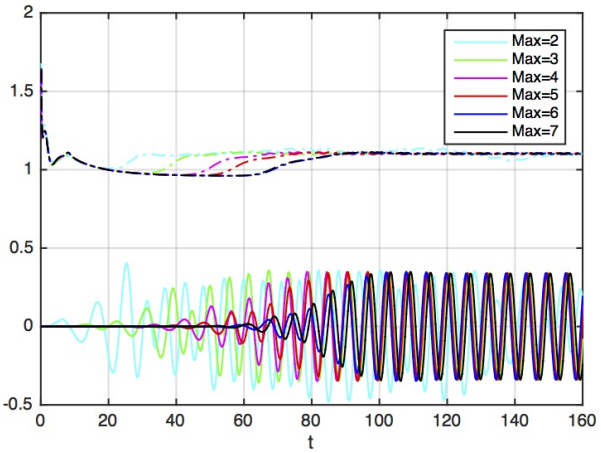

Figure 3: Temporal visualisation of the C_x and C_y coefficients for $Re = 200$, and $P = 2$ to 7.

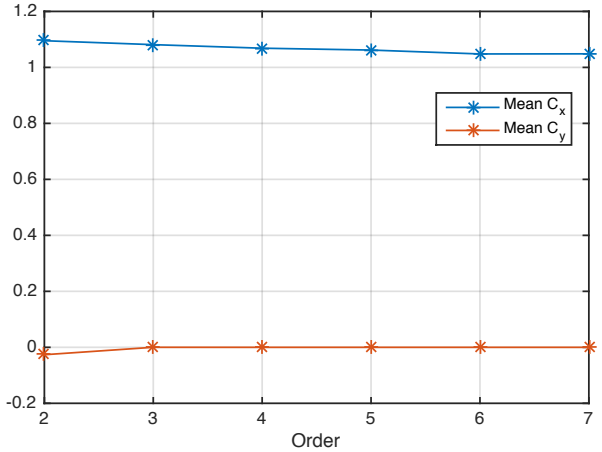

Figure 4: Visualisation of the mean of C_x and C_y coefficients for $Re = 200$, and $P = 2$ to 7.

This previous test validate our $p - type$ convergency, the following validate the $h - type$: we fix the maximum polynomial order $P = 6$ and compute the base flow (for $\alpha = 0°$ and $20°$) on the different meshes (see Tab. (2)).
Again, we see the different values of the coefficients in function of the dimensionless time t in Fig. (5) and their mean values in function of the different meshes in Fig. (6). We conclude that the "Mesh3" is already into the convergency zone, and so we chose its characteristics to compute our simulations in the next section.

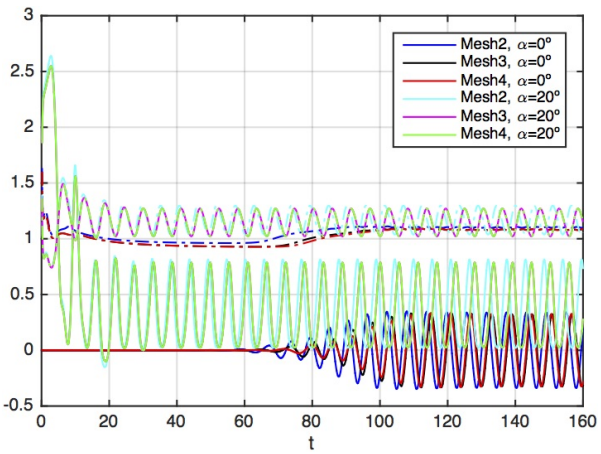

Figure 5: Temporal visualisation of the C_x and C_y coefficients for $Re = 200$, on $Mesh2$ to $Mesh4$.

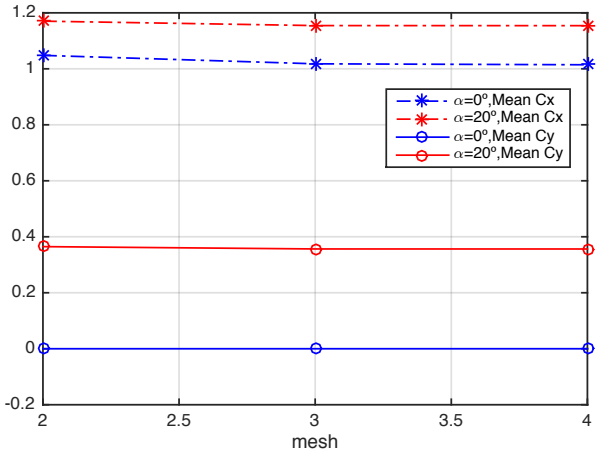

Figure 6: Visualisation of the mean of C_x and C_y coefficients for $Re = 200$, on $Mesh2$ to $Mesh4$.

The following section shows the velocity magnitude, vorticity, and pressure of the fluid flow around the body for different angles of attack: $\alpha = 0°, 5°, 10°, 15°$, and $20°$. The results are presented top-to-bottom following this order. These visualisations are extracted from the simulations at the moment where the vertical force coefficient C_y were maximum, during the steady state.

4. FLUID FORCES ACTING ON THE BODY

4.1 Velocity magnitude

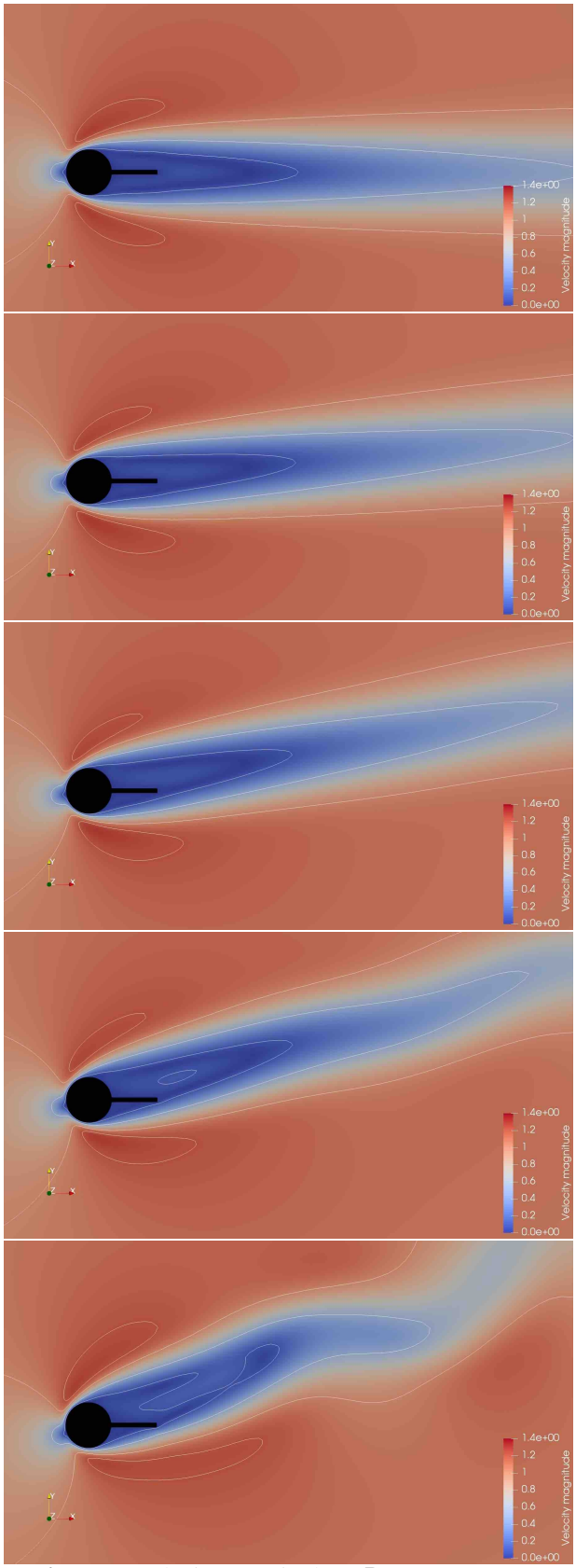

Figure 7: Velocity magnitude at $Re = 60$.

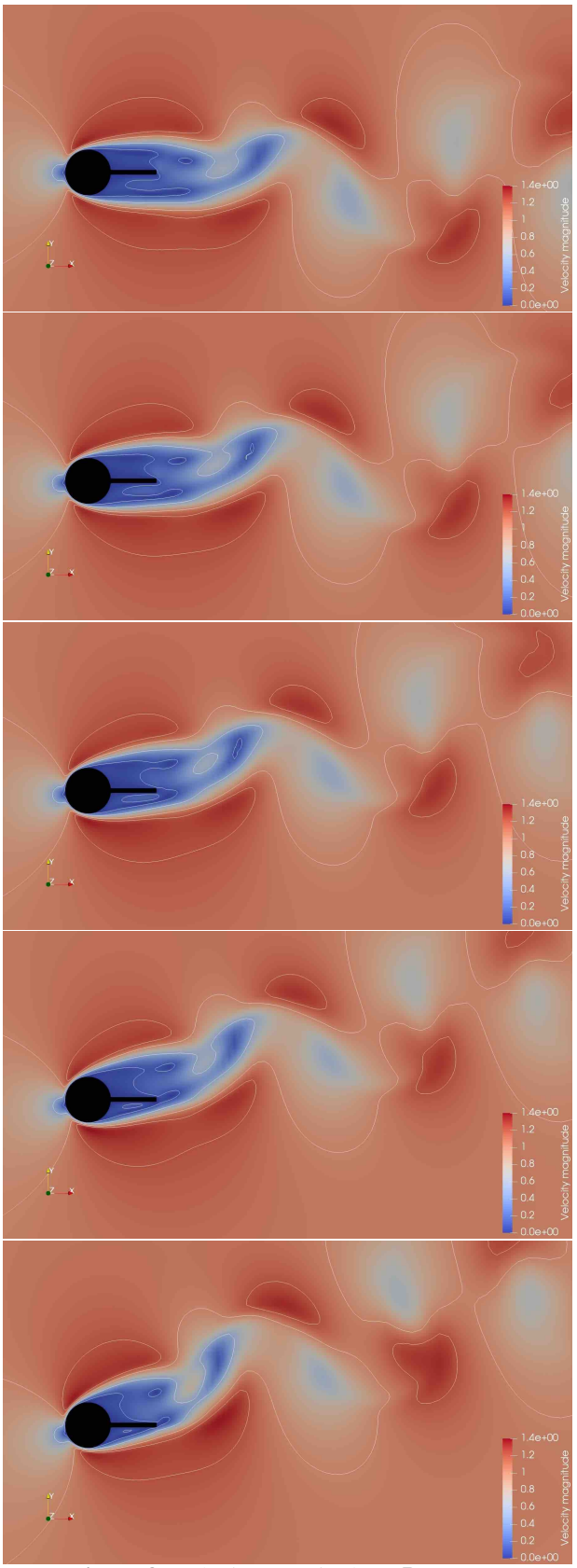

Figure 8: Velocity magnitude at $Re = 200$.

4.2 Vorticity

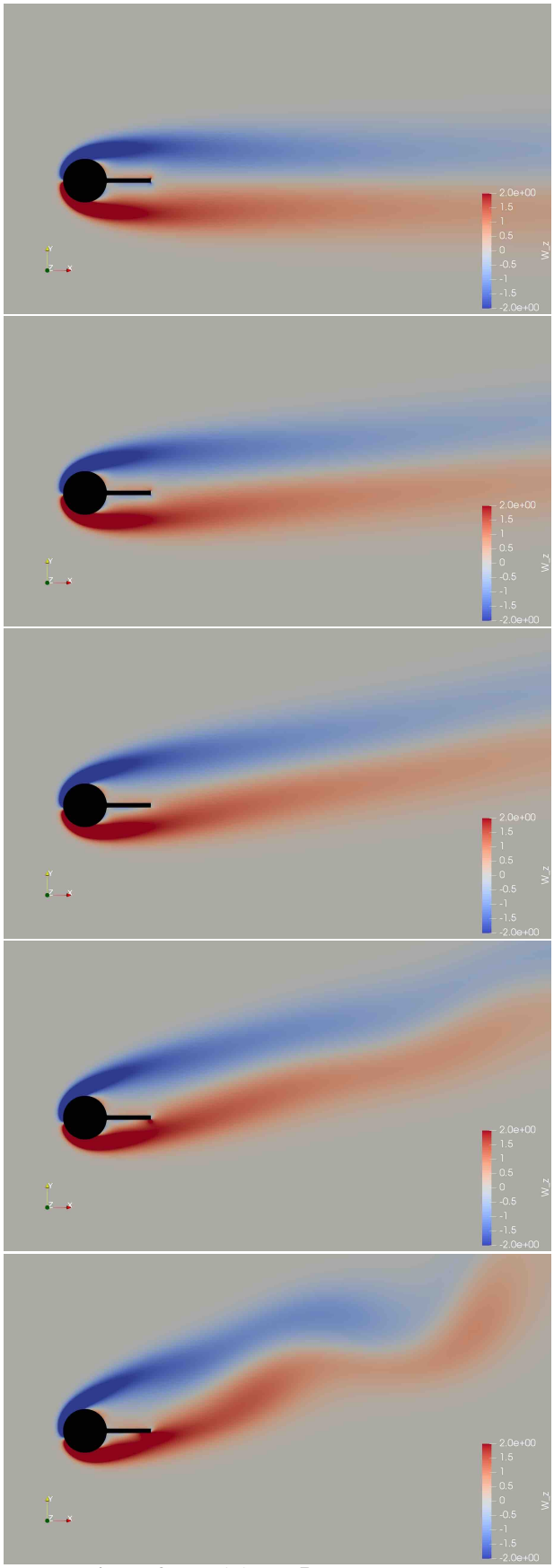

Figure 9: Vorticity at $Re = 60$.

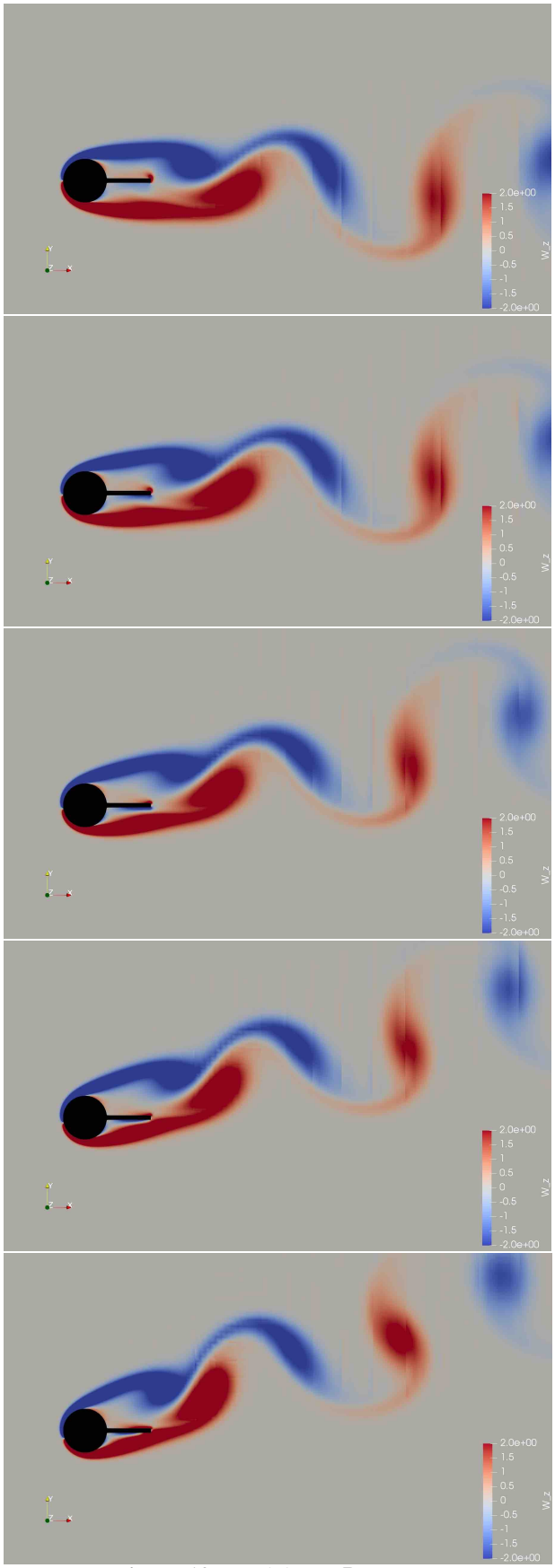

Figure 10: Vorticity at $Re = 200$.

4.3 Pressure

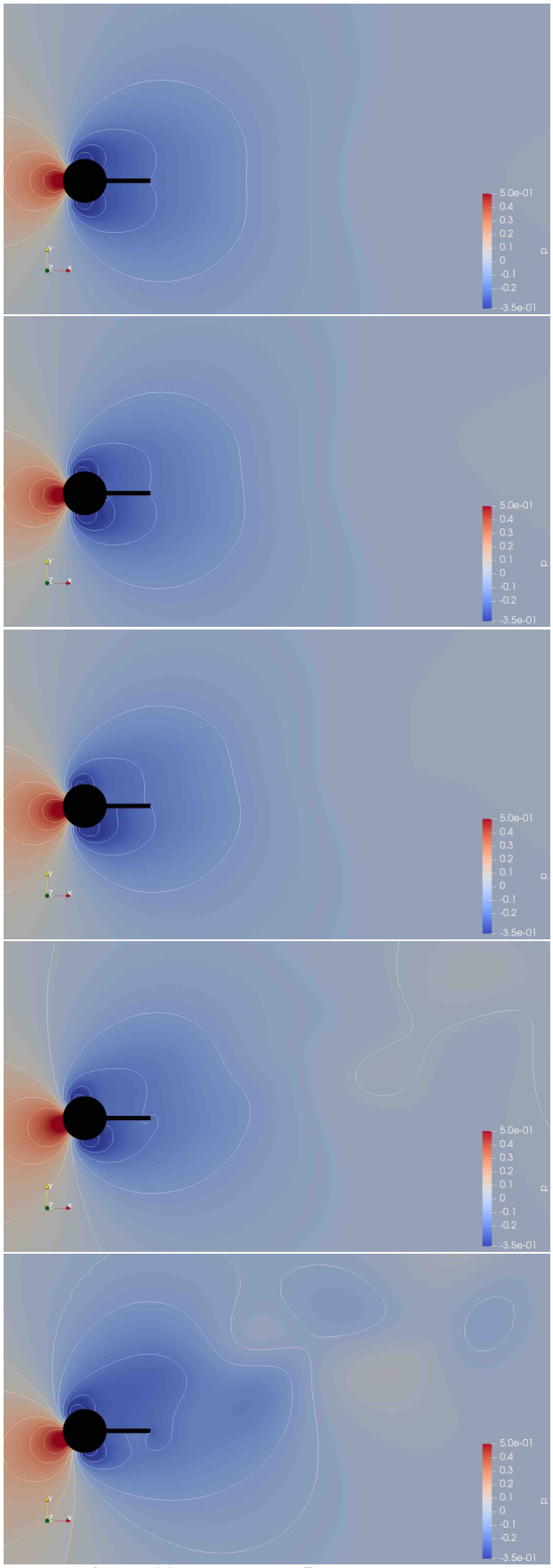

Figure 11: Pressure at $Re = 60$.

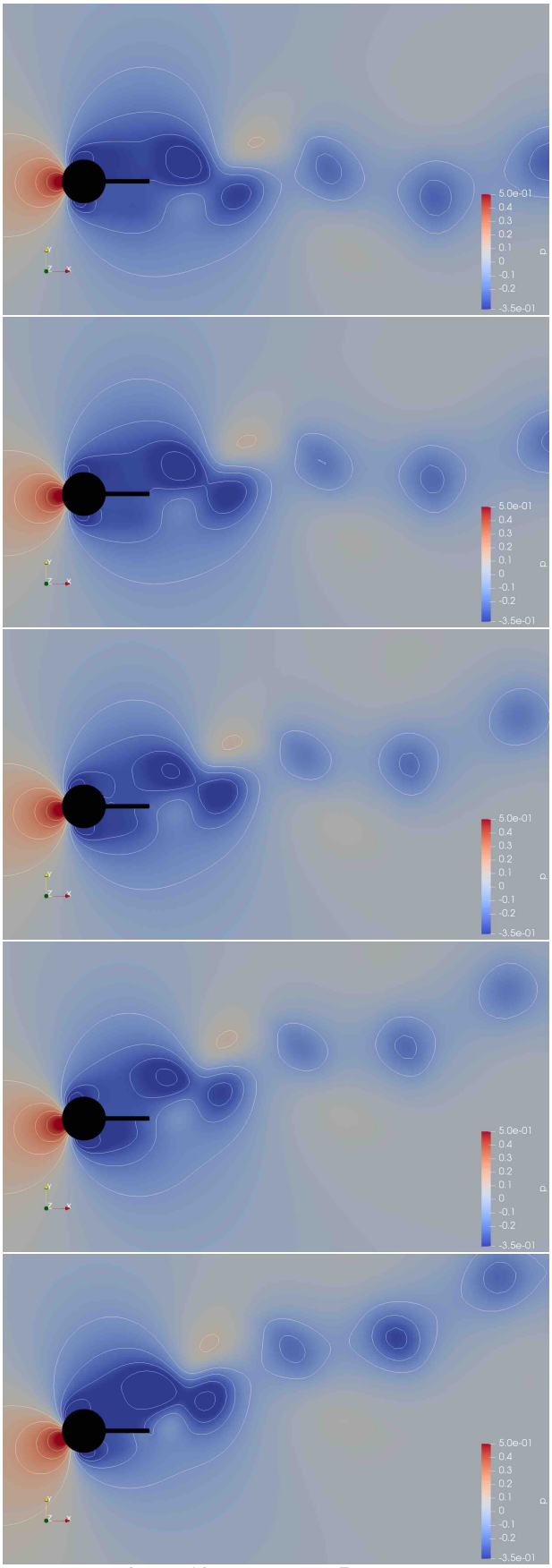

Figure 12: Pressure at $Re = 200$.

5. RESULTS AND DISCUSSIONS

In Fig. (7) to (12) we can see that the flow around the cylinder don't generate vortex shedding in steady state for all the angle of attack in the case of $Re = 60$. We only see apparition of vortex shedding starting from $\alpha = 15°$ while for $Re = 200$, the apparition of vortex shedding starts from $\alpha = 0°$. In this case, the cylinder acts as a bluff body for all the range of angle of attack, the mean velocity U is high enough to separate the flow locally at the surface of the body. We assume that for $Re = 60$, the splitter plate have the effect to keep the flow stick to the body until α reach the point that it make separate the flow at the very end of it.

Indeed, it make sense trigonometrically: $(D/2 + D).\sin(\alpha) \geq D/2 \Leftrightarrow \alpha \geq 20°$ is the angle of attack for which the end of the splitter plate is at a position greater than the cylinder's radius (in the direction parallel to the mean flow). Moreover, since the shear layer have a thickness $\hat{\delta} > 0$, it explain why the vortex shedding begin before $20°$. For higher values of Reynolds number, the flow already separate by itself.

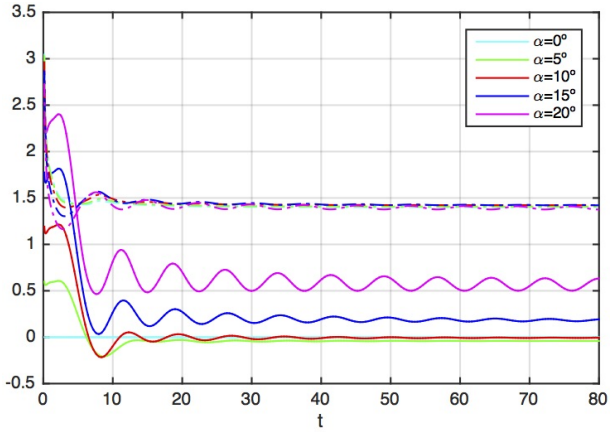

Figure 13: Temporal visualisation of the C_x and C_y coefficients for $Re = 60$.

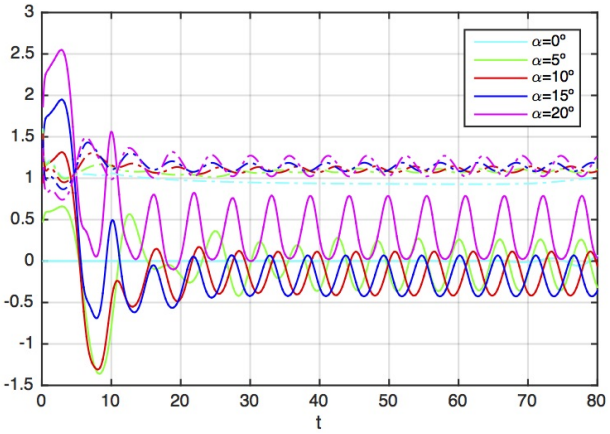

Figure 14: Temporal visualisation of the C_x and C_y coefficients for $Re = 200$.

Figures (13) and (14) confirm these assumptions by showing the temporal variations of the aerodynamics coefficients for $Re = 60$ and 200. We note the static tendency of C_y during the steady state until $\alpha = 15°$ for $Re = 60$, and the oscillations for the complete range of α in the case of $Re = 200$.

5.1 Polynomial interpolation

In Fig. (15) and Fig. (16) we can observe the evolution of the resulting force coefficients (here we talk in terms of total aerodynamic coefficients, resulting from the pressure and viscous contributions) C_x and C_y in function of the angle of attack α, here represented by the blue and red stars. Since we assume the geometry perfectly symmetric in relation to the (x, z) plane, we computed our base flow only for angle of attack positive ($\alpha = 0°$ to $20°$) and we deduct their negative values by a symmetric transformation. Represented here by the circles.

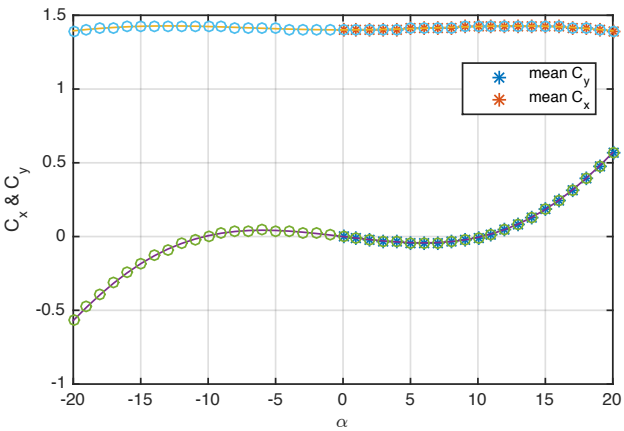

Figure 15: Arithmetic mean of C_x and C_y for Re=60, for $\alpha = -20°$ to $20°$.

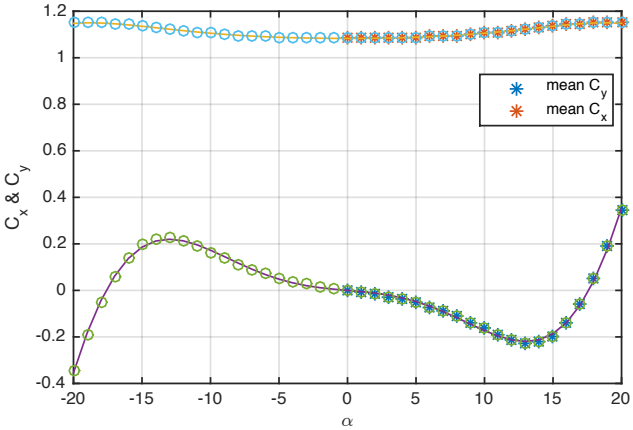

Figure 16: Arithmetic mean of C_x and C_y for Re=200, for $\alpha = -20°$ to $20°$.

The yellow and purple curves in Fig. (15) and Fig. (16) are the 7^{th} order polynomial interpolation ($P_7^x(x)$ and $P_7^y(x)$) of respectively C_x and C_y that we used to calculate the derivative of C_y around $0°$ (Fig. (17) and Fig. (18)). We calculated the polynomial interpolations by finding polynomials $P_n^x(x)$ and $P_n^y(x)$ of degree $n = 1$ to 7, that best fit (in a least-squares sense) the data in y (i.e. C_x and C_y).

Figures (17) and (18) presents the of the Den Hartog criterion's values for Reynolds 60 and 200. We compared these values depending of the data's order of interpolation. Clearly, for α between $-20°$ and $20°$, C_y is best interpolated by a polynomial of odd order (Fig. (15) and (16)). That's why we don't notice big differences between using an odd order of interpolation n and an even order of interpolation $n + 1$ for C_y, and we get this "step-function-like" for its derivative around 0.

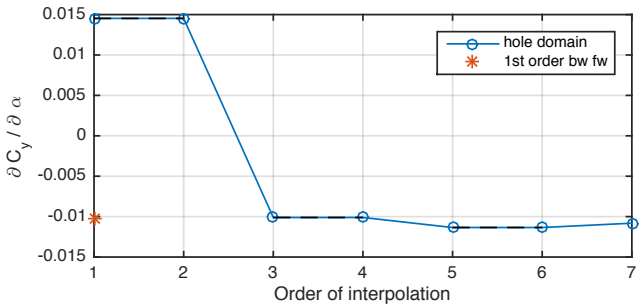

Figure 17: Values of the D.H. criterion regarding the order of interpolation of C_y, for $Re = 60$.

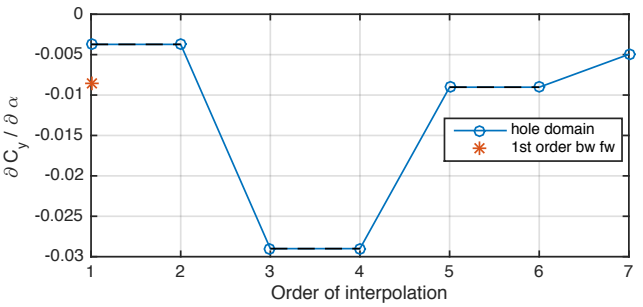

Figure 18: Values of the D.H. criterion regarding the order of interpolation of C_y, for $Re = 200$.

By this study we emphasise the importance to choose the right method of derivation. Figure (17) explicit the sign difference of the derivative value when $n < 3$, leading to a false interpretation of the stability. Here we compare the derivative value in zero of our interpolation scheme (blue circles) to the simple linear backward-forward derivate in zero (red star) that we use for reference.

In both cases, $\partial C_y/\partial\alpha|_{\alpha=0} < 0$: we aren't in potential plunge instability yet. We expect a potential instability around Reynolds = 1000, which will be investigated and discussed in a future work, as the torsional criterion of instability.

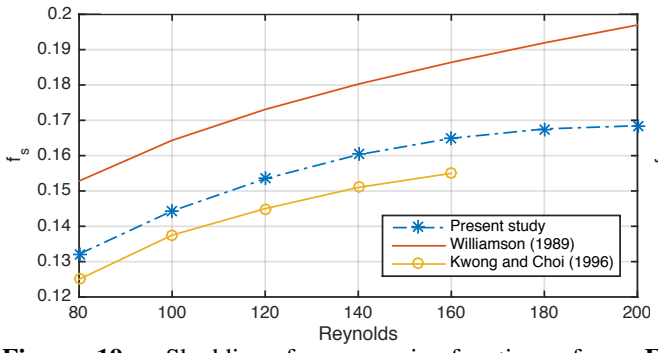

Figure 19: Shedding frequency in function of Reynolds for $\alpha = 0$.

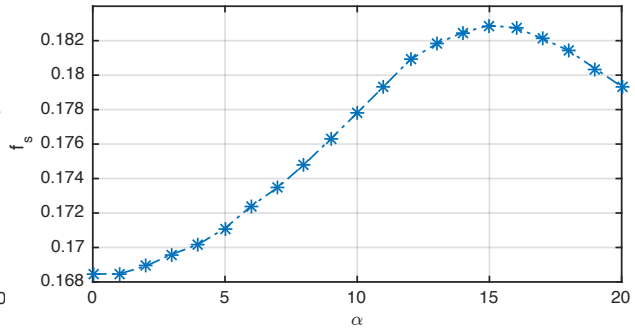

Figure 20: Shedding frequency in function of α for Reynolds = 200.

It is interesting to see that in Fig. (20) where we represented the shedding frequency in function of the angle of attack, for $Re = 200$, the range of values is close to the predicted Strouhal number $St = 0.2$. Indeed, since we choose to work with dimensionless scales ($U = 1$, $D = 1$), we get $St = f_s D/U = f_s$. If we compare these values to those of a circular cylinder in the same range of Reynolds number (Norberg, 2001), we get approximatively the same results: gently below 0.2. Furthermore, in Fig. (19), we compared the values of the shedding frequency during the steady state in function of the Reynolds number from the present simulations (from $Re = 80$ to 200, and for $\alpha = 0$), with the values from Kwon and Choi (1996) ($L/D \simeq 0.95$), and get a good coherency (we suppose the slight difference comes from the thickness difference of the splitter plate). We also compare these values to the analytical expression $St = -3.3265/Re + 0.1816 + 1.6e^{-4}Re$ (Williamson, 1989) and get the same shape for all the curves.

So far, we tested the Den-Hartog criterion of stability, through the Quasi-Steady theory. We see that with this type

of analyse, due to the complexity of the problem, the maximum we can predict is a potential instability (regarding the bounds of the amplitude in time). To go further, we will need the complete expression's value of ζ_T (see Eq. (13)) and examine its sign. Then, we will get the "real" criterion of instability, assuming we are still in the range of validity of the Quasi-Steady theory. Since we only will be able to give a value to the reduced velocity U^* when we will design a motion model (in order to extract f_n), we will take this criterion ($U^* > 20$) into account once the motion model found.

6. REFERENCES

Ahrens, James, Geveci, Berk, Law and Charles, 2005. "Paraview: An end-user tool for large data visualization." *Visualization Handbook*. ISBN-13: 978-0123875822.

Bearman, P.W., Gartshore, I.S., Maull, D.J. and Parkinson, G.V., 1987. "Experiments on flow-induced vibration of a square-section cylinder". *Journal of Fluids and Structures*, Vol. 1, pp. 19–34.

Blevins, R.D., 2001. *Flow-Induced Vibration*. Krieger publishing company, Krieger drive, Malabar, Florida 32950, 2nd edition.

Cantwell, C.D., Moxey, D., Comerford, A., Bolis, A., Rocco, G., Mengaldo, G., Grazia, D.D., Yakovlev, S., Lombard, J.E., Ekelschot, D., Jordi, B., Xu, H., Mohamied, Y., Eskilsson, C., Nelson, B., Vos, P., Biotto, C., Kirby, R.M. and Sherwin, S.J., 2015. "Nektar++: An open-source spectral/hp element framework". *Computer physics communications*, Vol. 192, pp. 205–219.

Den-Hartog, J.P., 1956. *Mechanical Vibrations*. McGraw-Hill Book Company, New York, McGraw-Hill, 4th edition.

Geuzaine, C. and Remacle., J.F., 2009. "Gmsh: a three-dimensional finite element mesh generator with built-in pre- and post-processing facilities." *International Journal for Numerical Methods in Engineering*, Vol. 79(11), pp. 1309–1331.

Karniadakis, G.E. and Sherwin, S.J., 2004. *Spectral/hp Elements Method for Computational Fluid Dynamics*. Oxford Science Publication, 2nd edition.

Kwon, K. and Choi, H., 1996. "Control of laminar vortex shedding behind a circular cylinder using splitter plates." *Phys. Fluids*, Vol. (8), pp. 479–486.

Nakamura, Y. and Mizota, T., 1975. "Torsional flutter of rectangular prisms". *Journal of Engineering Mechanics*, Vol. 101. Title from ASCE journal home page, viewed Jan. 12, 2000.

Norberg, C., 2001. "Flow around a circular cylinder: aspects of fluctuating lift." *Journal of Fluids and Structures*, Vol. (15), pp. 459–469.

Williamson, C.H.K., 1989. "Oblique and parallel modes of vortex shedding in the wake of a circular cylinder at low reynolds numbers." *J.. Fluid Mech.*, Vol. 206, pp. 579–627.

Zdravkovich, M., 1997. *Flow Around Circular Cylinders*, Vol. 1. Oxford Science Publication.

7. RESPONSIBILITY NOTICE

The authors are the only responsible for the printed material included in this paper.